Tidal signals in ocean-bottom magnetic measurements of the Northwestern Pacific: Observation versus prediction

Geophysical Journal International

Geophys. J. Int. (2014) **198,** 1096–1110 doi: 10.1093/gji/ggu190

GJI Geomagnetism, rock magnetism and palaeomagnetism

Tidal signals in ocean-bottom magnetic measurements of the Northwestern Pacific: observation versus prediction

N. R. Schnepf,[1] C. Manoj,[2,3] A. Kuvshinov,[4] H. Toh[5] and S. Maus[2,3]

[1] *Department of Earth, Atmospheric & Planetary Sciences, MIT, Cambridge, MA, USA. E-mail: nschnepf@mit.edu*
[2] *CIRES, University of Colorado at Boulder, Boulder, CO, USA*
[3] *National Geophysical Data Center, National Oceanic and Atmospheric Administration, Boulder, CO, USA*
[4] *Institute of Geophysics, ETH, Zurich, Switzerland*
[5] *Data Analysis Center for Geomagnetism and Space Magnetism, Kyoto University, Kyoto, Japan*

Accepted 2014 May 20. Received 2014 May 20; in original form 2013 April 23

SUMMARY

Motional induction in the ocean by tides has long been observed by both land and satellite measurements of magnetic fields. While these signals are weak (∼10 nT) when compared to the main magnetic field, their persistent nature makes them important for consideration during geomagnetic field modelling. Previous studies have reported several discrepancies between observations and numerical predictions of the tidal magnetic signals and those studies were inconclusive of the source of the error. We address this issue by (1) analysing magnetometer data from ocean-bottom stations, where the low-noise and high-signal environment is most suitable for detecting the weak tidal magnetic signals, (2) by numerically predicting the magnetic field with a spatial resolution that is 16 times higher than the previous studies and (3) by using four different models of upper-mantle conductivity. We use vector magnetic data from six ocean-bottom electromagnetic (OBEM) stations located in the Northwestern Pacific Ocean. The OBEM tidal amplitudes were derived using an iteratively re-weighted least-squares (IRLS) method and by limiting the analysis of lunar semidiurnal (M2), lunar elliptic semidinurnal (N2) and diurnal (O1) tidal modes to the night-time. Using a 3-D electromagnetic induction solver and the TPX07.2 tidal model, we predict the tidal magnetic signal. We use earth models with non-uniform oceans and four 1-D mantle sections underneath taken from Kuvshinov and Olsen, Shimizu *et al.* and Baba *et al.* to compare the effect of upper-mantle conductivity. We find that in general, the predictions and observations match within 10–70 per cent across all the stations for each of the tidal modes. The median normalized percent difference (NPD) between observed and predicted amplitudes for the tidal modes M2, N2 and O1 were 15 per cent, 47 per cent and 98 per cent, respectively, for all the stations and models. At the majority of stations, and for each of the tidal modes, the higher resolution ($0.25^\circ \times 0.25^\circ$) modelling gave amplitudes consistently closer to the observations than the lower resolution ($1^\circ \times 1^\circ$) modelling. The difference in lithospheric resistance east and west of the Izu–Bonin trench system seems to be affecting the model response and observations in the O1 tidal mode. This response is not seen in the M2 and N2 modes, thereby indicating that the O1 mode is more sensitive to lithospheric resistance.

Key words: Geomagnetic induction; Magnetic anomalies: modelling and interpretation; Marine electromagnetics.

1 INTRODUCTION

The ocean acts as a conducting fluid moving through the Earth's magnetic field. This induces electric fields, currents and secondary magnetic fields. These fields have been detected by ground, seafloor and satellite measurements (Larsen 1968; Cox *et al.* 1971; Sanford 1971; Chave *et al.* 1989; Tyler *et al.* 2003; Maus & Kuvshinov 2004). Due to their periodic nature, the magnetic signals generated by tides are relatively easy to detect and have been studied extensively (Malin 1970; McKnight 1995). Table 1 shows the major tidal modes with period near or within a day. Tides are driven by the gravitational forces caused by the relative movement of the Sun and Moon to the Earth. The observed tidal geomagnetic variations are due to a combination of electric currents in the ionosphere, ocean and their induced counterparts. Differential heating of the Earth's thermosphere by the Sun gives rise to tidal waves in the upper

Table 1. The periods of the different tidal modes. *Indicates the focus tidal modes of this study.

Tide	Period (hr)	Tide	Period (hr)
S6	4	M2*	12.421
S5	4.8	N2*	12.658
S4	6	K1	23.934
S3	8	S1	24
K2	11.967	P1	24.066
S2	12	O1*	25.819

atmosphere leading to a thermally driven dynamo in the ionosphere (Richmond 1995). These ionospheric currents cause the well-known diurnal variations in the geomagnetic field. Tidal gravitation forces cause concurrent motions in the ocean and ionosphere. The tidal waves give rise to motionally induced currents in both the ocean and ionosphere (although the ionosphere's currents are strongest during the day), that then induce secondary currents in the ocean and ionosphere.

Of the gravitational tides, the strongest contributions come from the lunar components (Egbert & Erofeeva 2002). This study chose to focus on three barotropic lunar tides, specifically the lunar semidiurnal (M2), the lunar elliptic semidiurnal (N2) and the lunar diurnal (O1) tidal modes, because they are among the strongest lunar tides and resolvable in simulations.

As discussed, the ocean tidal signals are a combination of the signals produced by both the ocean and ionosphere. To isolate the oceanic tidal fields, the Chapman–Miller method may be used on a complete time-series, assuming that the ionospheric tidal signal vanishes at midnight (Malin 1970). An alternative method is discarding the daytime data and assuming that ionospheric currents are negligible on the night side of the Earth (excluding the high latitudes). A recent study by Tyler *et al.* (2003) showed that the M2 tidal signal can be mapped from CHAMP satellite night side measurements. Their mapped signal was largely in agreement with a predicted motionally induced field produced from a satellite radar altimetry based ocean flow model (Egbert & Erofeeva 2002).

Simulations have been done to describe the magnetic fields produced by ocean tides (Hewson-Browne 1973; Kuvshinov & Olsen 2004; Dostal *et al.* 2012), however discrepancies between the predictions and observations exist (Maus & Kuvshinov 2004). Maus & Kuvshinov (2004) found that the M2 downward component differs from a prediction on a $1^\circ \times 1^\circ$ grid by a median value of 20 per cent among the seven observatories in the Indian Ocean region. Stations Alibag (ABG), Antananarivo (TAN), Charters Towers (CZT) and Learmonth (LRM) all had differences between 18 and 25.5 per cent, while the largest difference (675 per cent) was at Martin de Vivies (AMS). They found that the night-time CHAMP data over the Indian Ocean has an M2 amplitude of ∼0.84 nT, which is a 57 per cent match to the predicted value of 0.36 nT. It was unclear to them whether those discrepancies are due to inadequacies in data processing or modelling. Additionally, many of their sites were islands where distortion of tides may often be severe. The current study minimizes this issue by using submarine stations far from ocean–continent boundaries (Fig. 1).

While the tidal signals are weaker (less than 10 nT at the sea surface) than the main magnetic field, their persistent nature makes them an important source of noise to remove during geomagnetic field modelling (Maus *et al.* 2008). Hence, it is important to understand the source of discrepancies between numerical predictions and observations. Numerical predictions of magnetic signals due to ocean flows can most easily be fine-tuned for tidal flows. Their periodic nature enables isolating the tidal signals from other sources with relative ease. Once calibrated, our 3-D numerical code may be used to predict magnetic fields due to other types of ocean flows (e.g. circulation or tsunamis) by using a suitable flow model.

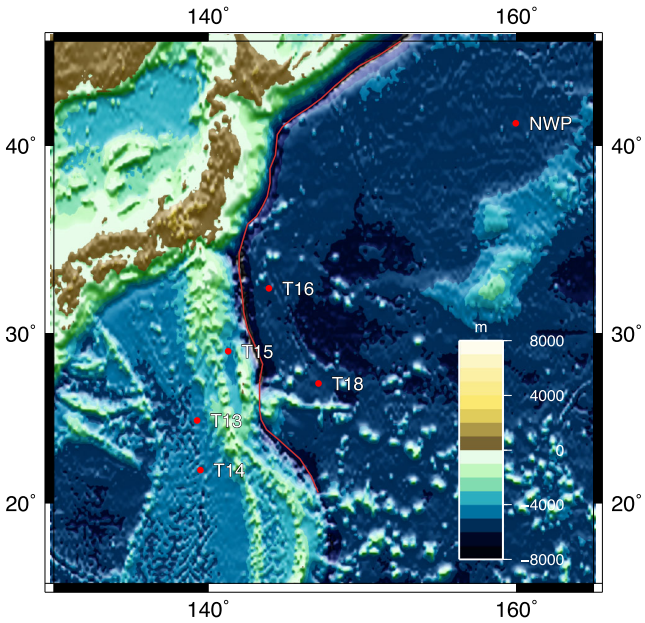

Figure 1. A map of the OBEMs. The red line denotes the Izu–Bonin trench system, separating the Philippine Sea mantle from the Pacific mantle (Baba *et al.* 2010).

To investigate the cause of discrepancies between observed and predicted tidal magnetic signals, we analysed data from six ocean-bottom electromagnetic (OBEMs) stations. The deep ocean measurements were expected to provide a low-noise and high-signal environment suitable for detecting the weak tidal magnetic signals. Using an outlier resistant, iteratively re-weighted least-squares (IRLS) method, we derived the dominant tidal modes in the magnetic data. For the numerical prediction, a 3-D electromagnetic (EM) induction solver (Kuvshinov *et al.* 2002) was used, as well as the TPX07.2 tidal model on a $0.25^\circ \times 0.25^\circ$ global grid (Egbert & Erofeeva 2002). The spatial resolution of the grid is 16 times larger than previous studies using a $1^\circ \times 1^\circ$ grid (Kuvshinov & Olsen 2004; Maus & Kuvshinov 2004).

We describe the OBEM stations and data processing in Section 2. Section 3 describes the spectral properties of the data. We present the results of our estimation of the dominant tidal components in Section 4. The numerical prediction of the tidal magnetic signals is discussed in Section 5. We use four previously published conductivity models for the upper mantle (up to 1000 km depth) for our simulations. Finally, we compare the observations and predictions, followed by a discussion of the results and summary.

2 DATA AND DATA PROCESSING

Data from six ocean-bottom electromagnetometer (OBEM) observatories in the Northwestern Pacific (Fig. 1 and Table 2) were used. The stations collect data every minute for ∼1 yr using a vector fluxgate magnetometer to determine the northward (X), eastward (Y) and downward (Z) components (Toh *et al.* 2006; Baba *et al.* 2010). The primary aim of the measurements by Baba *et al.* (2010) was to understand the deep geoelectrical structure of the ocean-subsurface;

Table 2. The location and time span of each ocean-bottom electromagnetic station.

	Lat.	Lon.	Depth	Data span
Toh *et al.* (2006)				
NWP	41.10°N	159.96°E	5580 m	2001-08-01 to 2002-08-01
Baba *et al.* (2010)				
T13	24.98°N	139.30°E	4794 m	2005-10-01 to 2006-11-30
T14	22.00°N	139.50°E	4945 m	2005-10-01 to 2006-11-30
T15	29.00°N	141.32°E	4026 m	2005-10-01 to 2006-11-30
T16	32.52°N	143.96°E	5408 m	2007-11-01 to 2008-11-30
T18	27.14°N	147.17°E	5594 m	2006-11-01 to 2007-11-30

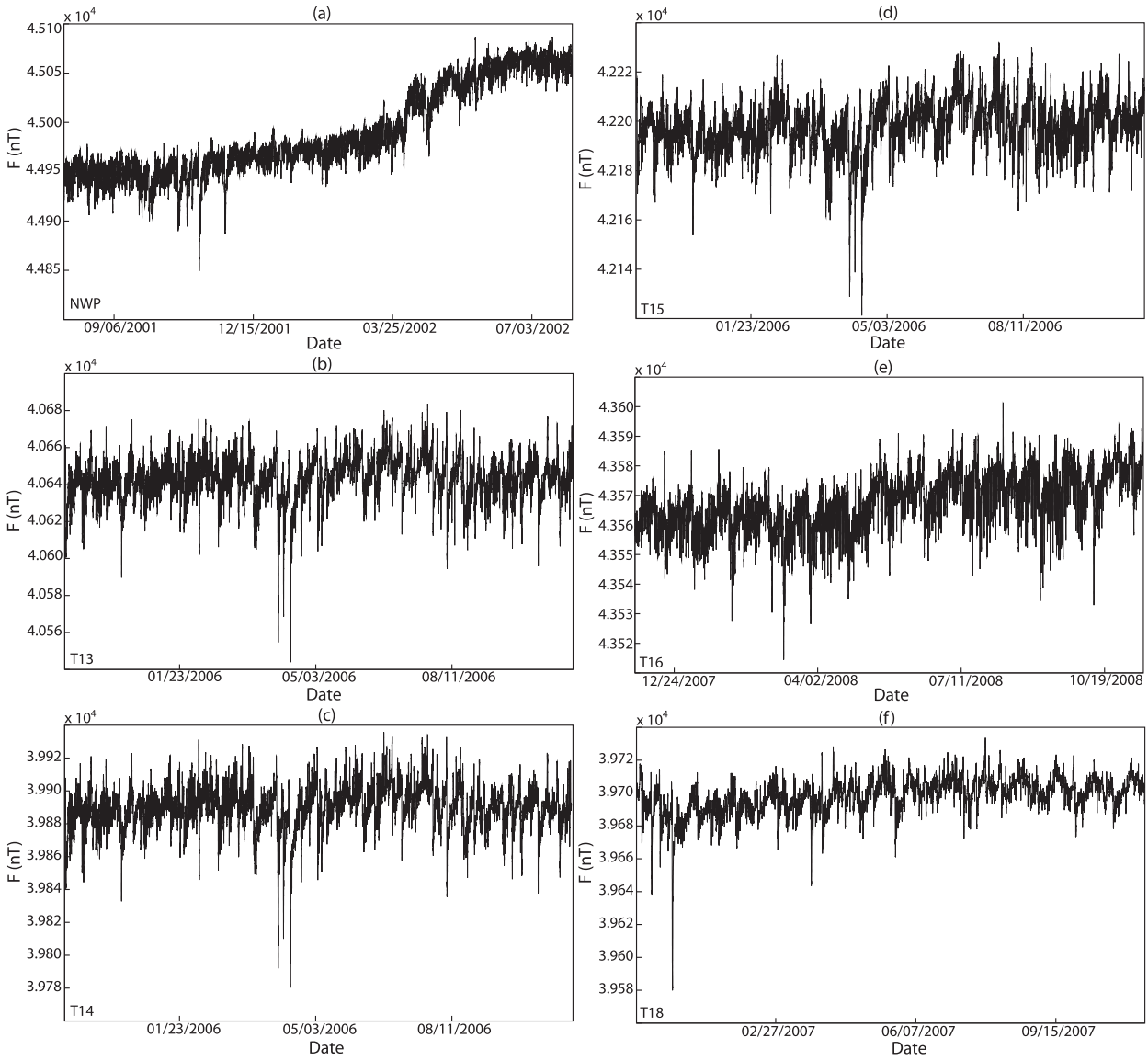

Figure 2. The raw scalar field time-series at each station: (a) NWP; (b) T13; (c) T14; (d) T15; (e) T16; (f) T18.

because the study was a campaign run, each station only produced data for a year. While NWP has been active for longer than a year, we only had access to data from 2001-08-01 to 2002-08-01. The timeframes of each data station are shown in Table 2 and the data are shown in Fig. 2. The predominant signal of the time-series is that of daily variation (forced by the thermally driven ionospheric dynamo), with intermittent spikes due to magnetic storms.

Although the attitude of the OBEMs is initially determined, the OBEM platform may slowly move or tilt during the measurements. To accommodate for this, each of the stations monitored the changes in tilt. We treat the tilt or movement during OBEM deployment as a possibility and do not want to add a possible unknown factor to our study. To remove these uncertainties in measurements (however small they may be) and to focus on comparing

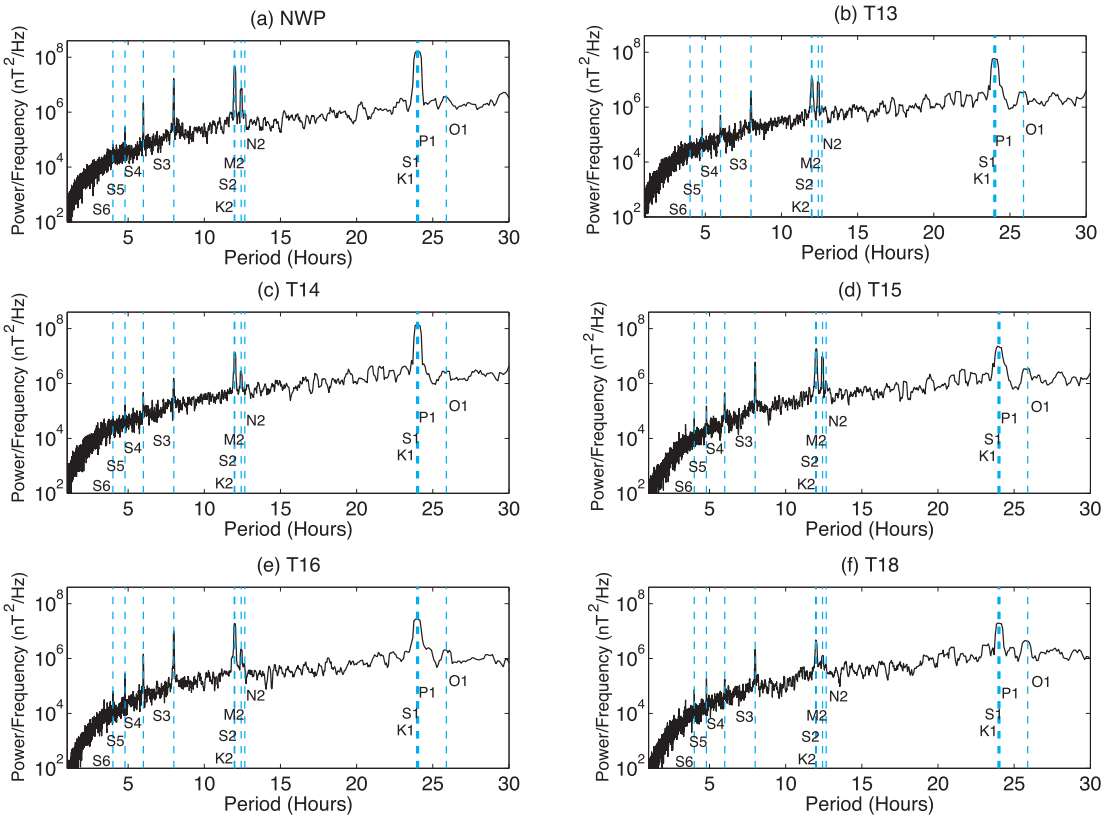

Figure 3. The power spectral density (power per frequency) shown for the range of tidal values.

results to numeric simulations, the following analysis is limited to the scalar field component F, which was calculated from both the vector components as well as measured by NWP's ocean-bottom magnetometers.

3 POWER SPECTRAL DENSITY (PSD) OF THE DATA

The PSD is the magnetic field power signal per unit frequency. Our aim here is to look at the power of the signal as a function of period. The PSD was determined by employing Thomson's multitaper method (Thomson 1982) on the entire length of each data set. Instead of averaging subdivided segments like the traditional Welch's periodogram method, the multitaper method minimizes the estimation bias by obtaining multiple independent estimates from the same sample. In the Thomson (1982) method, the time-series is multiplied by a set of discrete Slepian prolate spheroidal sequence (dpss) tapers. These dpss tapers are orthogonal sequences in the frequency domain that form single taper periodograms. These are then averaged as an estimate of the PSD. The goal here is to present the overall picture of the spectrum; the specific values for different tidal modes cannot be accurately determined with a time-series this short as the spectral resolution depends on the length of the time-series.

We use the MATLAB (Version R2013b, 2013) method 'pmtm' to calculate the Thomson spectral estimate. A time-halfbandwidth of $nw = 4$ was used to control the frequency resolution of the multitaper estimate. In this process, MATLAB automatically uses $2nw - 1$ Slepian tapers to produce the PSD estimate. For our time-halfbandwith, this results in seven Slepian tapers. The raw spectral estimates were adaptively averaged using Thomson's (1982) adaptive frequency-dependent weights. More information on the adaptive weights is available from Thomson (1982) and Prieto *et al.* (2007). Deviating from Thomson (1982), no attempts were made to reshape the spectrum at the tidal frequencies.

The PSD as a function of period (range of 1–30 hr) is plotted in Fig. 3. For periods greater than 10 hr, all the stations have nearly the same level of the background power. Due to the increased attenuation of signals in the conductive ocean water, deeper stations (such as T18) show lower power for shorter periods than the shallower stations (such as T14). The background signal at NWP is generally higher than the rest of the stations, probably because it was measured during the solar active period of 2000–2001. For example, the average solar flux value (F10.7) when NWP was measured was 165 solar flux units (sfu, 10^{-22} W m^{-2} Hz^{-1} at 10^{-7} cm; Dmitry 2007) as compared with the 2005–2006 period's average solar flux value of ∼80 sfu. However, we do not expect that the difference in solar activity levels affect our night-time ocean dynamo signals and hence the data from different campaigns are directly comparable. The estimated background spectral power is in good agreement with the mid-latitude geomagnetic power spectra by Olsen (2007). The dominant source for signals in this period range are the ionospheric and magnetospheric current systems. Superimposed on the background spectra are the six well-defined peaks generated by the ionosphere and ocean tidal dynamo system due to the gravitational forces from the Sun and Moon. In this paper, we focus on the lunar tidal dynamo effects. In the PSD plot, we can clearly see the M2 and O1 signals. The N2 signal is not as strong, but it is also visible in these plots.

4 ESTIMATION OF MAGNETIC TIDAL MODE AMPLITUDE

The PSD estimates of the tides include contributions both from the ionospheric dynamo (caused by the tidally forced winds within the conductive ionosphere), the ocean dynamo system and their induced signals within both the ocean and land. The night-time ionospheric E-region conductivity is an order or two less than its daytime value, so one way to separate the ionospheric signal from the ocean dynamo is to limit the analysis to night-time only (where night-time is defined as 18:00–06:00 local time; Kelley 1989). However, the multitaper method is not suitable to analyse data with gaps. Instead, the tidal harmonics can be directly fit to the data in a least-square (LS) sense. To remove long-term trends from the estimations, we also fit period of half a year, a year and the period of nodal modulation (18.6 yr). This method can estimate values at an exact frequency, as well as provide an estimate of the error.

Each magnetic measurement y_i can be defined by a mathematical model given by,

$$y_i = \sum_n \{A(n)\cos[2\pi\nu(n)t_i] + B(n)\sin[2\pi\nu(n)t_i]\} + C, \quad (1)$$

where, $i = 1, \ldots, N$ is a positive integer indicating each data point, n is a positive integer indicating each tidal mode, $\nu(n)$ is the frequency of the signal considered (number of cycles per day) and t is the time in days. The coefficients $A(n)$, $B(n)$ and C are estimated by fitting the above model to the data. The LS method works best for data that do not contain a large number of random errors with extreme values—for example, data with a Gaussian distribution.

In order to minimize the effect of outliers in the data, we use an IRLS method. The IRLS method punishes the outliers by weighing them down in each successive iteration (Huber 1981). This was done using the 'robustfit' method as implemented in MATLAB (Version R2013b, 2013) to estimate the tidal amplitudes. For the weight function, we use Tukey's biweight (bisquare) with a default tuning constant, $t = 4.685$, which is a good general-purpose choice for robust regression. At first, the algorithm determines initial estimates of the coefficients using ordinary least squares. For each iteration, the residuals $r = \mathbf{resid}/(ts\sqrt{1-h})$ are computed, where **resid** is the vector of residuals from the previous iteration, h is the vector of leverage values (hat matrix diagonal) from the least-squares fit and s is an estimate of the standard deviation of the error term given by $s = \mathrm{MAD}/0.6745$, where MAD is the median-absolute-deviation of the $n - p$ largest residuals from the previous iteration. The constant 0.6745 was chosen to convert data units into population units for the normal distribution. We then compute the new weights followed by the weighted least-square estimates of coefficients. These steps are iterated until the coefficients converge or until some maximum iteration limit is reached. In all cases, the iterations converged before the preset iteration max of 50 reached. The variance–covariance matrix of the model parameters is estimated as $\sigma^2(X^TX)^{-1}$, where σ is an approximation of the residual standard deviation using the theory of robust regression and incorporating the final robust weights and X is computed using the final robust weights. The final variance–covariance matrix is given in the Appendix. Table 3 shows the result of the estimation.

The amplitudes of the daytime M2 signals range from 0.54 to 2.14 nT, whereas for the night-time, the amplitudes range from 0.21 to 1.60 nT. The night-time M2 amplitudes are in general smaller than the daytime estimates, but only by 10–30 per cent. The only exception is station T14, where the night-time signal strength exceeds the daytime value. At the majority of the stations, the ocean M2 signals are stronger than the ionospheric M2 signals. This is in agreement with the analysis by Malin (1970) on geomagnetic data from the British islands. Day and night estimates of N2 and O1 modes also have similar relationships.

Table 3. The observed amplitudes (Column Obs.) for the M2, N2 and O1 tidal modes are given here with their standard error values (Column SE). The corresponding predicted values using the $0.25^\circ \times 0.25^\circ$ grid (SM1) and a $1^\circ \times 1^\circ$ grid (SM2) outlined in Section 5, as well as the predicted values using different 1-D conductance models, are also given here. The column PHS uses the Philippine Sea mantle model and the column PAC uses the Pacific mantle model from Baba *et al.* (2010). The column KO uses the 1-D conductivity model of Kuvshinov & Olsen (2006). All the amplitudes given are in units of nT.

Station	Obs.	SE	SM1	SM2	PHS	PAC	KO
			The M2 tidal mode				
NWP	1.60	0.0287	1.79	1.73	1.44	1.58	1.68
T13	1.51	0.0327	1.68	1.30	1.66	1.38	1.41
T14	0.81	0.0358	0.69	0.72	1.11	0.71	0.75
T15	1.60	0.0283	0.98	0.80	1.92	1.39	1.33
T16	0.76	0.0193	0.96	0.98	1.34	0.97	0.95
T18	0.21	0.0266	0.60	0.65	0.90	0.57	0.65
			The N2 tidal mode				
NWP	0.44	0.0287	0.30	0.30	0.28	0.28	0.30
T13	0.49	0.0327	0.37	0.32	0.38	0.33	0.34
T14	0.35	0.0358	0.21	0.22	0.28	0.20	0.22
T15	0.45	0.0283	0.26	0.22	0.41	0.32	0.32
T16	0.10	0.0193	0.22	0.23	0.30	0.23	0.23
T18	0.17	0.0265	0.20	0.22	0.28	0.21	0.23
			The O1 tidal mode				
NWP	0.77	0.0287	0.28	0.24	0.58	0.31	0.32
T13	0.48	0.0327	0.56	0.50	0.74	0.60	0.58
T14	0.56	0.0358	0.46	0.41	0.63	0.47	0.47
T15	0.49	0.0284	0.35	0.21	0.66	0.47	0.47
T16	1.12	0.0193	0.21	0.14	0.59	0.28	0.23
T18	1.19	0.0266	0.36	0.26	0.69	0.41	0.44

The standard error of each amplitude was calculated from the square root of the model variance–corvariance matrix diagonal elements (Appendix). The median standard error for each tidal mode was 0.0285 nT, with a range of 0.0193–0.0358 nT. In general, for the M2 mode the standard error was 1.3–6.6 per cent of the found amplitude. The O1 mode's standard error was also small relative to the found amplitudes: in all cases it was within 10 per cent. Similarly, the N2 mode's standard error values ranged from 3.5 to 6.6 per cent of the found amplitude.

5 FORWARD PREDICTION

We predict the magnetic fields due to tidal ocean flow using the numerical solution described in Kuvshinov *et al.* (2002). This solution simulates the EM fields excited by arbitrary sources in spherical models of the Earth with a 3-D distribution of electrical conductivity. Using this approach and a time harmonic dependence given by $e^{-i\omega t}$, Maxwell's equations in the frequency domain,

$$\frac{1}{\mu_0}\nabla \times \mathbf{B} = \sigma\mathbf{E} + \mathbf{j}^{\mathrm{ext}} \quad (2)$$

and

$$\nabla \times \mathbf{E} = i\omega\mathbf{B}, \quad (3)$$

are reduced to a contracting integral equation (e.g. Pankratov *et al.* 1997). Here, $\mathbf{j}^{\text{ext}}$ is the exciting current (in this case, $\mathbf{j}^{\text{ext}}$ is the electric current induced by the tidal flow), σ is the conductivity distribution of the model and μ_0 is the magnetic permeability of the free space. The electric fields in the 3-D spherical model are determined by resolving the integral equation. Finally the magnetic field **B** within the ocean layer at the observation points is calculated using Green's function formalism. For a detailed description of the 3-D EM simulation as applied to motionally induced signals, see Kuvshinov & Olsen (2004) and Kuvshinov (2008). The exciting current, $\mathbf{j}^{\text{ext}}$, is calculated as

$$\mathbf{j}^{\text{ext}} = \sigma_w \left(\mathbf{U} \times \mathbf{B}^m\right), \tag{4}$$

where $\sigma_w = 3.2\ \text{S m}^{-1}$ is the mean sea water conductivity, **U** is the depth integrated velocity due to ocean tides taken from the $0.25^\circ \times 0.25^\circ$ resolution global tidal model, TPX07.2 (shown in Fig. 6; Egbert & Erofeeva 2002) and $\mathbf{B}^m$ is the magnetic field derived from the IGRF-11 (Finlay *et al.* 2010) using software that automatically selects the correct model epoch for a given date. The 3-D model consisted of a thin spherical layer of laterally varying conductance at the Earth's surface and a radially symmetric spherical conductivity underneath. The conductance of the surface layer is obtained by combining the contributions from sea water and sediments. The conductance distribution of the sea water has been calculated by multiplying the ETOPO5 (5 min × 5 min) bathymetry with mean sea water conductivity and interpolating to a $0.25^\circ \times 0.25^\circ$ grid. Conductance of the sediments is based on the global sediment thicknesses given by the $1^\circ \times 1^\circ$ map of Laske & Masters (1997). The sediments' conductivity is calculated by a procedure similar to that described in Everett *et al.* (2003). For the underlying spherical conductor (laterally homogeneous), we chose four previously published models instead of assuming an insulating mantle (e.g. Vivier *et al.* 2004). They are Shimizu *et al.* (2010, SM), Kuvshinov & Olsen (2006, KO) and the Philippine Sea mantle model (PHS) and the Pacific mantle model (PAC) from Baba *et al.* (2010). For the rest of the paper, we refer to these models by their corresponding abbreviations. Fig. 4 shows the 1-D conductivity profiles we use. Note that in the papers of Shimizu *et al.* (2010) and Kuvshinov & Olsen (2006)

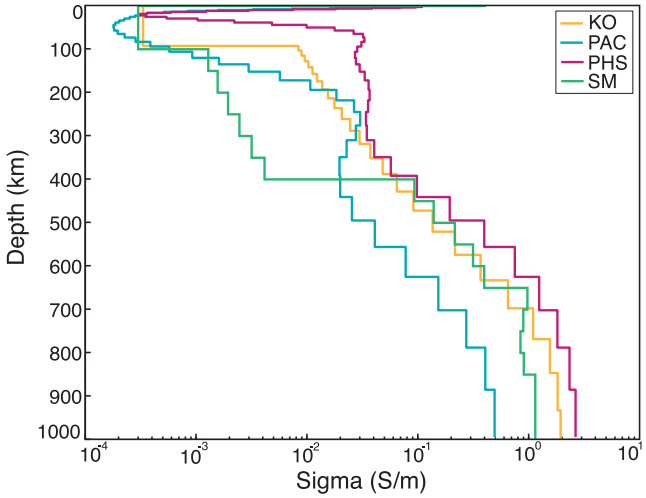

Figure 4. The orange line shows the 1-D global section model produced by Kuvshinov & Olsen (2006), the blue line shows the 1-D Pacific mantle model produced by Baba *et al.* (2010), the magenta line shows the 1-D Philippine Sea mantle model produced by Baba *et al.* (2010) and the green line shows the 1-D conductivity section produced by Shimizu *et al.* (2010) for the North Pacific.

when estimating 1-D sections they fixed the conductivity of the upper 100 km to preferred values. These preferred values—2000 Ω-m and 3000 Ω-m, respectively—are consistent with the values obtained from analysis of coastal magnetic data (*cf.* Kuvshinov *et al.* 1999) and electric cable data (*cf.* Kuvshinov *et al.* 2006b). These models in general show a resistive lithosphere underlain by a mantle whose conductivity increase with depth, the models differ considerably in detail. For example, PHS shows a very thin resistive layer in the lithosphere as compared to the other models. Model SM shows a relatively resistive upper mantle as compared to the other models. For the periods considered, the conductivity for depths exceeding 1000 km depth is not relevant.

By altering the periods, the magnetic field is simulated on a global grid of $0.25^\circ \times 0.25^\circ$ resolution for each of the tidal components listed in Table 1 (SM1). To understand the effect of grid resolution, we additionally predict the signals on a $1^\circ \times 1^\circ$ resolution. For this we use 1-D model by Shimizu *et al.* (2010; SM2). The predicted amplitudes produced by these different models may be seen in Table 3. The different conductivity models are shown in Fig. 4.

We obtain the scalar amplitudes by projecting the predicted magnetic field vector **B** on to the unit vector $\frac{\mathbf{B}^m}{|\mathbf{B}^m|}$ in the direction of the main magnetic field (as determined by the International Geomagnetic Reference Field) at each gridpoint:

$$\triangle F = \mathbf{B} \cdot \frac{\mathbf{B}^m}{|\mathbf{B}^m|}. \tag{5}$$

This makes the projected $\triangle F$ directly comparable with the scalar observations by OBEMs. Maps of the predicted M2, N2 and O1 signals are given in Fig. 5. The global pattern of the tidal magnetic fields closely follows the radial component of the geomagnetic field and the depth integrated tidal velocities (eq. 4, also shown in Fig. 6). The magnetic signals are negligible along the dip equator due to the weak geomagnetic radial component. The strength of the magnetic signals increases towards the magnetic poles. While the pattern of the scalar anomaly is in agreement with a previous prediction by Tyler *et al.* (2003), the higher resolution of the present simulation brings out detailed local structures of the tidal magnetic field. As the periods of M2 and N2 tides are close (Table 1), their induced magnetic signals have similar patterns. However, the amplitudes of the M2 signals are about five times stronger than N2 signals (also shown by their much faster median velocity values in Fig. 6). The pattern of the predicted O1 (period of 25.819 hr) is significantly different from that of M2 and N2, as expected from its very different velocity map (Fig. 6). While the fields mostly vary within 0.5–1 nT, isolated signals exceeding 4 nT are predicted in the regions close to the geomagnetic poles. For this study, we focus on a smaller region in the Northwestern Pacific Ocean.

6 COMPARISON TO PREDICTION OF TIDAL OCEAN FLOW SIGNAL

From the forward prediction (shown in Fig. 5), the expected average amplitude in the magnetic field due to M2 tides varies by 10 nT globally for all the model configurations we use. The large-scale features of the map are in agreement with the $1^\circ \times 1^\circ$ global simulations by Maus & Kuvshinov (2004, fig. 1). However, the new simulation shows many small spatial scale features that have not previously been resolved. For example, the series of higher amplitude anomalies along the Aleutian Islands in the Bering sea was not resolved in any of the previous simulations.

To compare the observations with the predicted values, we plotted the predicted and observed amplitudes on a subset of the global

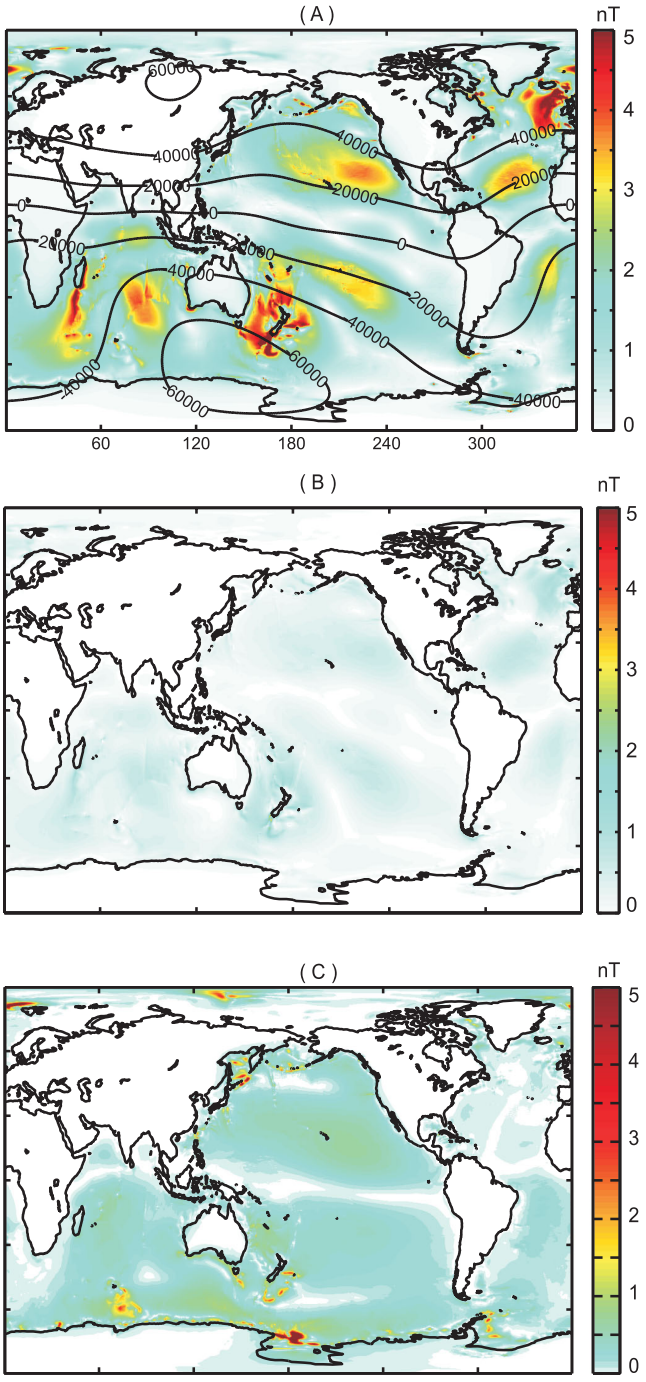

Figure 5. The predicted scalar anomalies on 0.25° × 0.25° resolution using 1-D conductivity model by Shimizu *et al.* (2010) due to (a) the M2 tide with contour lines of the vertical component of the Earth's main field $\mathbf{B}^m$ from the International Geomagnetic Reference Field, (b) the N2 tide and (c) the O1 tide.

map (Figs 7–9). The values are also listed in Table 3. The estimated amplitudes of M2 tide-induced magnetic signals are very close to the predicted amplitudes at four out of the six stations considered. The normalized percent difference (NPD) was computed for each station by computing the difference between the estimated (E) and predicted (P) amplitude and dividing that by the standard deviation of the model's predicted values (σ_P):

$$\mathrm{NPD} = 100 \cdot \frac{|E - P|}{\sigma_P}. \quad (6)$$

The median NPD for M2, N2 and O1 at all stations, and for all models, was 15, 47 and 72 per cent, respectively. For stations NWP, T13 and T14 the M2 mode's normalized differences are within ∼14 per cent of the predicted values for all the models except SM2 and PHS (16 and 20 per cent, respectively). Despite some of the discrepancies, considering that the stations are spread out over a large region (there is a maximum distance of 2800 km between NWP and T14) with different signal-to-noise ratios, such high agreement for the other stations is remarkable. The predicted amplitudes from all model configurations for the M2 mode are very close to each other at all stations, except at T15 where the normalized difference exceeds 60 per cent for the SM2 model. At station T15, the observed amplitude is about 1.6 nT but the predicted amplitudes from models vary between 0.8 and 1.9 nT. The spread of the predicted amplitudes is largest at this station both for M2 and N2 modes.

The observed N2 tidal signals are within 10–85 per cent for the predicted values. At T15, all the models except for SM2 have an NPD under 85 per cent, ranging from within 13 per cent (using PHS) to 67 per cent (using SM1). The observed N2 signals exceed predictions, except at stations T16 and T18. For stations T13, T14 and T15, the PHS model gives the values closest to the estimation. For stations NWP, T16 and T18, the SM1 model is closer.

The O1 tidal signals have a larger range of normalized differences, from matching within 5 per cent at T15 using KO and PAC to above 300 per cent difference at T16 and T18 using SM2. For the O1 signals, the difference between the observation and predictions are significantly larger for stations east of the Izu–Bonin trench system (shown in Fig. 1). For example, at stations NWP, T16 and T18, the observations are 103–316 per cent larger than all the predictions. At NWP, the model PHS (40 per cent) is the only one to match below 100 per cent difference. For all stations, the model SM2 has high NPDs, exceeding 48 per cent at all stations except T13 where it is within 7 per cent.

7 DISCUSSION

7.1 Effect of model resolution

Our objective here is to discuss the influence of grid resolution on the predicted amplitudes. We have modelled the tidal signals on a 1° × 1° (SM2) and 0.25° × 0.25° (SM1) grids while keeping all other parameters the same. We have used the model from Shimizu *et al.* (2010) for the 1-D conductivity model. In general, their differences are not significant compared to the general variance of all predictions. In most cases, the amplitudes from the higher resolution grid are closer to the observed amplitudes (Table 3 and Figs 7–9). The difference between 1° × 1° and 0.25° × 0.25° modelling for the M2 and N2 modes is most pronounced at T15 and T13, which are close to the Izu–Bonin trench system. The main contributors to the exciting currents (eq. 4) are the depth integrated tidal flow velocity and the radial component of the geomagnetic main field. The geomagnetic main field has very large spatial scales and varies smoothly (Fig. 5a). It is evident from Figs 6 and 10 that the tidal amplitudes are maximum near site T15. The gradient of the flow for both components U and V are also relatively high at T15. Hence, it is possible that the resolution of the tidal flow model is causing a part of the difference. The other change in model input is the difference in the resolution of the conductance map. The sea water contribution to the conductance map is derived from a 5′ × 5′ ETOPO bathymetry multiplied by the salinity and re-gridded to a 0.25° × 0.25° resolution. The contribution from the

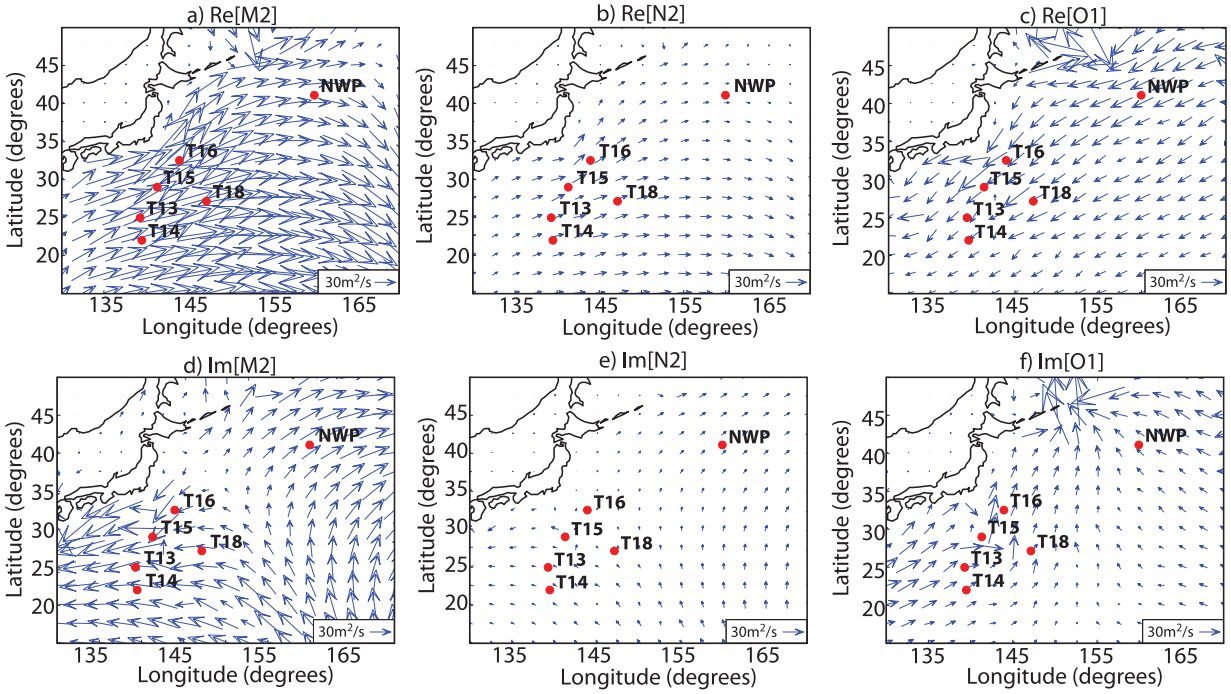

Figure 6. TPX07.2 tidal flow velocity maps for M2's (a) real and (d) imaginary velocity components, N2's (b) real and (e) imaginary velocity components, and O1's (c) real and (f) imaginary velocity components. The stations are denoted with the red circles and the median velocity value for a given component is shown in each plot's legend.

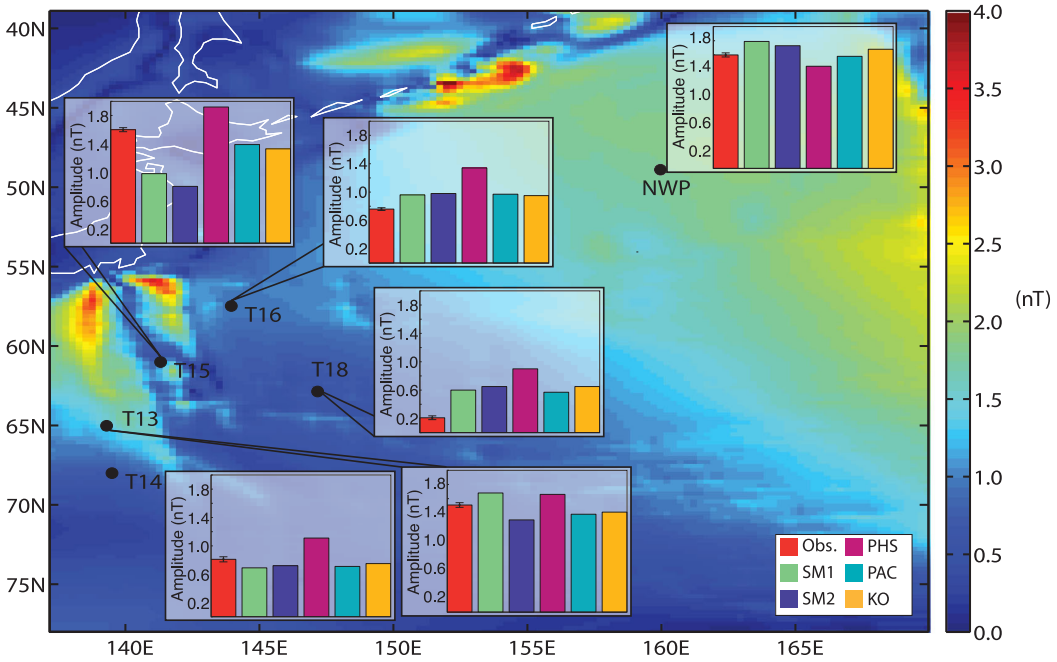

Figure 7. Night-time observed versus predicted amplitudes for the M2 tidal mode at each station, with the predicted (SM1) M2 amplitudes shown in the background. Error bars are shown for the observed amplitude bar at each station.

sedimentary rocks beneath the ocean bottom was derived from a 1° × 1° sedimentary thickness map by Laske & Masters (1997) and 1-D North Pacific conductivity section by Shimizu *et al.* (2010). The largest contribution to the electrical conductance comes from the ocean water. It is then possible that the unmodelled variations in the bathymetry/sediment thickness might have also contributed to the difference between SM1 and SM2. In the case of T13 and T15, this is more pronounced due to its proximity to the Izu–Bonin trench system (Fig. 1). Hence we argue that it is important to model the ocean magnetic signals on higher resolution grids if the gradient of bathymetry or tidal flow is significant in the immediate vicinity to the observation site.

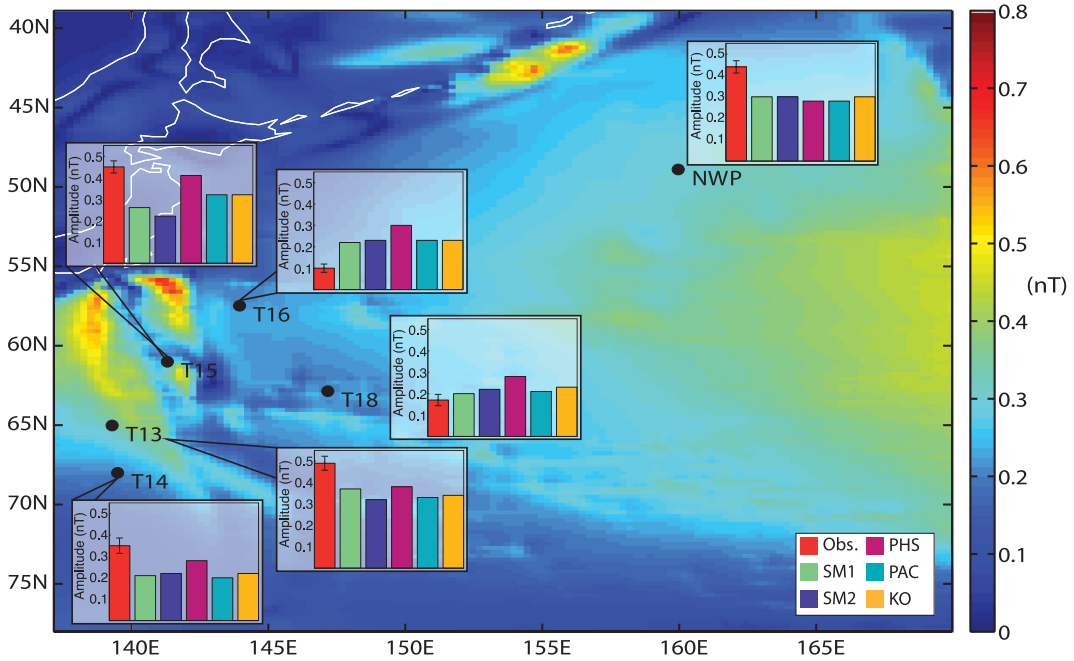

Figure 8. Night-time observed versus predicted amplitudes for the N2 tidal mode at each station with the predicted (SM1) N2 amplitudes shown in the background. Error bars are shown for the observed amplitude bar at each station.

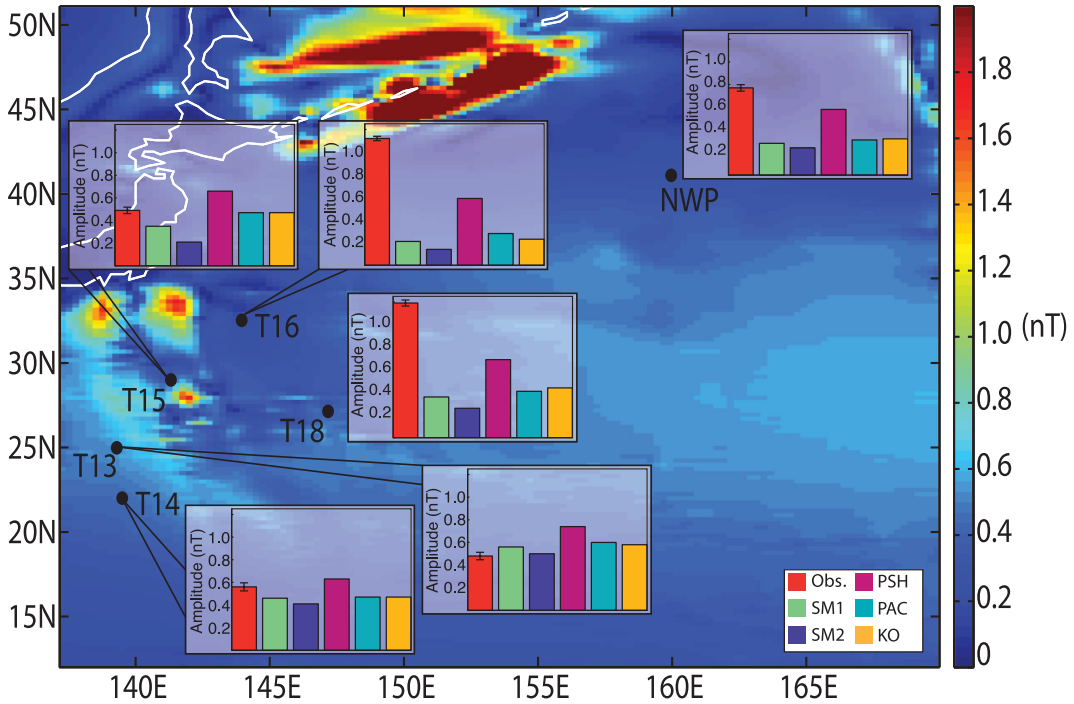

Figure 9. Observed versus predicted amplitudes for the O1 tidal mode at each station with the predicted (SM1) O1 amplitudes shown in the background. Error bars are shown for the observed amplitude bar at each station.

7.2 Effect of upper-mantle conductivity

We have modelled the tidal signals using four 1-D conductivity models of the upper mantle (Fig. 4). While the Kuvshinov & Olsen (2006) model was derived from global data and hence represents a global average, the other three models are derived from Pacific Ocean data. The tidal amplitudes using models KO and PAC gives almost the same amplitudes for all the modes at each of the stations. The 1-D KO and PAC models have very similar conductivities for the upper mantle. They also are similar to SM for the upper 100 km, however they are about an order of magnitude higher than that of SM for depths between 100 and 400 km. Several authors suggest a large difference between the PHS and the Pacific mantle in the conductivity of the upper 200 km (e.g. Baba *et al.* 2010) and many have also observed that the lithospheric resistance is sensitive to the electromagnetic fields induced by ocean flow (Larsen 1968; Cox *et al.* 1971; Kuvshinov *et al.* 2006a; Baba *et al.* 2010, 2013). Toh

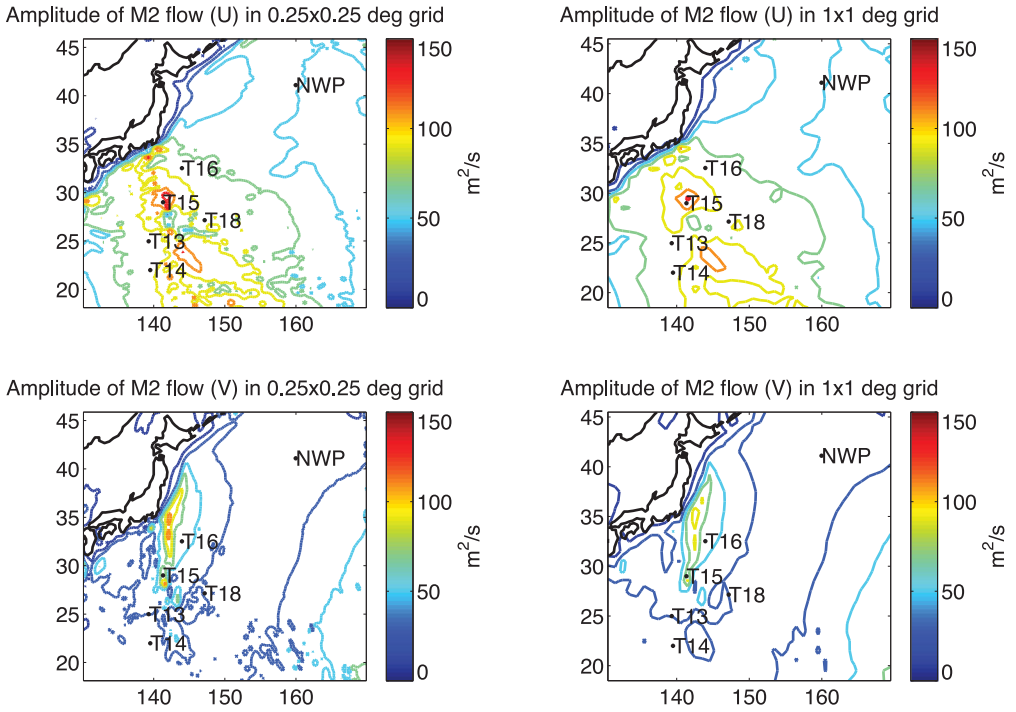

Figure 10. Tidal depth-integrated flow velocity contours on 0.25° × 0.25° resolution (left-hand panels) and on 1° × 1° resolution (right-hand panels).

(1993) finds that the resistive layer in the upper 200 km of the Pacific is four times as thick as that of the Philippine Sea, with the border along Izu–Bonin arc system (Fig. 1). This is reflected in the models PAC and PHS. The stations T13, T14, T15, are in the Philippine sea region and their N2 observations are closer to the predictions of the PHS model. On the other hand, for the stations east of the Izu–Bonin arc system (T16 and T18), the PHS model consistently overestimates the N2 amplitude. For these stations, the 1-D models with a more resistive upper mantle (>200 km depth) give the closer fit for the N2 estimated amplitudes.

For the M2 mode, the PAC and KO models predict amplitudes closest to the observations across all the stations, with average absolute NPD of 14 per cent and 13 per cent respectively. This is surprising since we expected the PHS model to better predict the Philippine Sea stations, as in the case of N2. We do not have an immediate explanation for this.

For Pacific stations, the observed O1 is higher than all the predictions. Except at T13, the PHS model is relatively closer to the observations at all the stations. Although the PHS model gives a better fit with observations for the N2 mode in the Philippine Sea, the modelling results could not consistently prove that some models are better than others for the M2 and O1 modes. The O1 observations at NWP, T14, T16 and T18 more closely match the predictions that have lower lithospheric resistances (PHS) than the models with a thicker and more resistive lithosphere (PAC). This finding is consistent with a new study by Baba *et al.* (2013). Using sea bottom magnetometer data near station NWP, they find that the resistive layer (100 km) under the North Pacific ocean is comparable to the Philippine Sea (PHS) but significantly thinner than at the area of the Bonin Trench (PAC). Hence the motional induction by O1 may be a better sensor for lithospheric resistance than by the M2 or N2 modes.

Nodal modulation is caused by the change in angle between the plane of the Moon's orbit and the Earth's equatorial plane over a period of 18.6 yr. To correct for this in the observed tidal amplitudes the period of nodal modulation was included in the IRLS method. The effect of nodal modulation is largest for O1 tides where we saw changes in amplitude reaching up to 23 per cent. For the M2 mode, incorporating the nodal modulation period varied amplitudes by 0.75–2.5 per cent. These results are consistent with the expectation that, depending on the modulation phase, the effect can reach up to 18 per cent for the O1 mode, whereas for the M2 mode, the effect is about 3 per cent of the observed amplitude (Shaw & Tsimplis 2010).

In all the models considered, we allow the conductivity to vary laterally in the upper most layer to account for the effect of oceanic water and sediments in the ocean bottom and continents. Below this layer, we used four different 1-D conductivity models (Fig. 4) to predict the tidally induced magnetic signals. In order to study the effect of the hypothetic lithospheric resistivity discontinuity at the ocean–continent boundary on the predicted tidal signals, we performed additional forward modelings in which we assigned a set of different values for lithospheric resistivity below oceans and continents. However we observed only minor differences (not shown in the paper) in the predicted signals in the region of interest. Another possible influence on the results is the subduction zone short circuit for the electric currents from the ocean to the deep mantle which is not included in the models. While we do not think that this short circuit is playing a major role for the tidal signals in the region, this topic indeed deserves a separate study which we aim to pursue in the future.

8 CONCLUSIONS AND OUTLOOK

The PSD revealed six well-defined peaks generated by the ionosphere and ocean tidal dynamo system due to the gravitational forces from the Sun and Moon. The lunar semidiurnal (M2), the

lunar elliptic semidiurnal (N2) and lunar diurnal (O1) signals are clearly defined (see Fig. 3), however these peaks include contributions both from the ionospheric dynamo, the ocean dynamo system and their induced signals within both the ocean and land. The ionospheric signal was separated from the ocean dynamo by limiting the analysis to night-time only and directly fitting the tidal harmonics to the data by using IRLS.

From the forward prediction (shown in Fig. 5), the expected average amplitude in the magnetic field due to M2 tides varies by 10 nT globally. The large-scale features of the map are in agreement with the $1^\circ \times 1^\circ$ global simulations by Maus & Kuvshinov (2004, fig. 1). However, the new simulation shows many small spatial scale features that have not previously been resolved.

The median NPD between observed and predicted amplitudes for the tidal modes M2, N2 and O1 were 15, 47 and 72 per cent, respectively, for all the stations and models. There is an indication that the upper-mantle conductivity influences the lunar tidal ocean dynamo signals. The difference in upper-mantle conductivity east and west of the Izu–Bonin trench system seems to be affecting the model response and observations in the N2 tidal mode. However, we do not see a similar behaviour in the M2 and O1 modes. In the majority of stations, for each of the modes, the higher resolution ($0.25^\circ \times 0.25^\circ$) modelling gave amplitudes consistently closer to the observations than the lower resolution ($1^\circ \times 1^\circ$) modelling.

The implications of these results are important for analysing the data from the upcoming *Swarm* satellite mission to survey the Earth's magnetic field, and will also be useful for future geomagnetic field modelling. Ocean magnetic field amplitudes may be constrained from satellite measurements (Tyler *et al.* 2003; Maus & Kuvshinov 2004; Manoj *et al.* 2006), and improved modelling capabilities will increase our ability to identify non-tidal ocean flow using Swarm satellite measurements.

In general, these results will assist correcting data for a known field contribution, namely the tidal ocean flow. Furthermore, as satellites' capability to map the crustal field increases, it will be more important to correct the crustal fields for predicted signals of steady ocean circulation.

From here, it will be important to keep working towards higher resolution grids (for both conductance and tidal flow) for ocean flow studies. High-resolution maps of sediment thickness are available (Whittaker *et al.* 2013) and should be incorporated into the prediction of the fields using high-resolution local and global grids. The high-resolution sedimentary thickness data are available from the National Geophysical Data Center (http://ngdc.noaa.gov/mgg/sedthick/index.html). The availability of higher resolution bathymetric data and tide models would also be useful for incorporation into the field predictions. For example, future studies will want to consider using Cheng & Andersen's (2010) global ocean tide model, DTU10, since it has a finer resolution of $0.125^\circ \times 0.125^\circ$. The next natural step from here is to look at components of both the magnetic and electric fields, as well as their phases, and to analyse more data from the region.

Our study also shows the importance of using realistic and laterally inhomogeneous upper-mantle conductivity models for ocean tidal modelling. Current availability of such models is limited to a few areas.

ACKNOWLEDGEMENTS

We thank Hisashi Utada (Earthquake Research Institute, University of Tokyo) and Noriko Tada (Japan Agency for Marine-Earth Science and Technology) for providing the data for this study. NRS is grateful to the National Oceanic & Atmospheric Administration's Hollings Scholarship Program for making this research possible. We would also like to thank one anonymous reviewer and Alan Chave for useful comments and critiques, as well as Andrew Roberts for the ncquiverref.m script.

REFERENCES

Baba, K., Utada, H., Goto, T.-N., Kasaya, T., Shimizu, H. & Tada, N., 2010. Electrical conductivity imaging of the Philippine Sea upper mantle using seafloor magnetotelluric data, *Phys. Earth planet. Inter.,* **183**(1–2), 44–62.

Baba, K., Tada, N., Zhang, L., Liang, P., Shimizu, H. & Utada, H., 2013. Is the electrical conductivity of the northwestern Pacific upper mantle normal? *Geochem. Geophys. Geosyst.,* **14**(12), 4969–4979.

Chave, A.D., Filloux, J.H. & Luther, D.S., 1989. Electromagnetic induction by ocean currents: BEMPEX, *Phys. Earth planet. Inter.,* **53**(3–4), 350–359.

Cheng, Y. & Andersen, O.B., 2010. *Improvement in Global Ocean Tide Model in Shallow Water Regions*. *Poster, SV,* OSTST, pp. 1–68.

Cox, C.S., Filloux, J.H. & Larsen, J.C., 1971. Electromagnetic studies of ocean currents and electrical conductivity below the ocean-floor, in *The Sea,* pp. 637–693, ed. Maxwell, A., Wiley.

Dmitry, K., 2007. Virtual observatory for SPIDR metadata. Tech. Rep., Space Physics Interactive Data Resource, National Geophysical Data Center, Boulder, CO.

Dostal, J., Martinec, Z. & Thomas, M., 2012. The modelling of the toroidal magnetic field induced by tidal ocean circulation, *Geophys. J. Int.,* **189**(2), 782–798.

Egbert, G.D. & Erofeeva, S.Y., 2002. Efficient inverse modeling of barotropic ocean tides, *J. Atmos. Ocean. Technol.,* **19,** 183–204.

Everett, M.E., Constable, S. & Constable, C.G., 2003. Effects of near-surface conductance on global satellite induction responses, *Geophys. J. Int.,* **153**(1), 277–286.

Finlay, C.C. *et al.*, 2010. International Geomagnetic Reference Field: the eleventh generation, *Geophys. J. Int.,* **183**(3), 1216–1230.

Hewson-Browne, R.C., 1973. Magnetic effects of sea tides, *Phys. Earth planet. Inter.,* **7,** 161–166.

Huber, P.J., 1981. *Robust Statistics,* Wiley.

Kelley, M.C., 1989. *The Earth's Ionosphere: Plasma Physics and Electrodynamics,* Academic Press.

Kuvshinov, A.V., 2008. 3-D global induction in the oceans and solid earth: recent progress in modeling magnetic and electric fields from sources of magnetospheric, ionospheric and oceanic origin, *Surv. Geophys.,* **29**(2), 139–186.

Kuvshinov, A. & Olsen, N., 2004. 3-D modelling of the magnetic fields due to ocean tidal flow, in *Earth Observation with CHAMP: Results from Three Years in Orbit,* pp. 359–365, eds Reigber, C., Lühr, H., Schwintzer, P. & Wickert, J., Springer-Verlag.

Kuvshinov, A. & Olsen, N., 2006. A global model of mantle conductivity derived from 5 years of CHAMP, Ørsted, and SAC-C magnetic data, *Geophys. Res. Lett.,* **33**(18), L18301, doi:10.1029/2006GL027083.

Kuvshinov, A.V., Avdeev, D.B. & Pankratov, O.V., 1999. Global induction by Sq and Dst sources in the presence of oceans: bimodal solutions for non-uniform spherical surface shells above radially symmetric earth models in comparison to observations, *Geophys. J. Int.,* **137**(3), 630–650.

Kuvshinov, A., Junge, A. & Utada, H., 2006a. 3-D modelling the electric field due to ocean tidal flow and comparison with observations, *Geophys. Res. Lett.,* **33**(6), L06314, doi:10.1029/2005GL025043.

Kuvshinov, A., Sabaka, T. & Olsen, N., 2006b. 3-D electromagnetic induction studies using the Swarm constellation: mapping conductivity anomalies in the Earths mantle, *Earth Planets Space,* **58,** 417–427.

Kuvshinov, A.V., Avdeev, D.B., Pankratov, O.V., Golyshev, S.A. & Olsen, N., 2002. Modelling electromagnetic fields in a 3D spherical Earth using a fast integral equation approach, in *3D Electromagnetics,* pp. 43–54, eds Zhdanov, M.S. & Wannamaker, P.E., Elsevier Sci.

Larsen, J.C., 1968. Electric and magnetic fields induced by deep sea tides, *Geophys. J. R. astr. Soc.,* **16,** 47–70.

Laske, G. & Masters, G., 1997. A global digital map of sediment thickness, *EOS, Trans. Am. geophys. Un.,* **78,** F483.

Malin, S., 1970. Separation of lunar daily geomagnetic variations into parts of ionospheric and oceanic origin, *Geophys. J. R. astr. Soc.,* **21,** 447–455.

Manoj, C., Kuvshinov, A. & Maus, S., 2006. Ocean circulation generated magnetic signals, *Earth Planets Space,* **58,** 429–437.

Maus, S. & Kuvshinov, A., 2004. Ocean tidal signals in observatory and satellite magnetic measurements, *Geophys. Res. Lett.,* **31,** L15313, doi:10.1029/2004GL020090.

Maus, S. *et al.*, 2008. Resolution of direction of oceanic magnetic lineations by the sixth-generation lithospheric magnetic field model from CHAMP satellite magnetic measurements, *Geochem. Geophys. Geosyst.,* **9**(7), 1–10.

McKnight, J.D., 1995. Lunar daily geomagnetic variations in New Zealand, *Geophys. J. Int.,* **122,** 889–898.

Olsen, N., 2007. Natural Sources for Electromagnetic Induction, in *Encyclopedia of Geomagnetism and Paleomagnetism,* pp. 696–700, eds Gubbins, D. & Herrero-Bervera, E., Springer-Verlag.

Pankratov, O.V., Kuvshinov, A.V. & Avdeev, D.B., 1997. High-performance three-dimensional electromagnetic modelling using modified Neumann series. Anisotropic Earth, *J. Geomagn. Geoelectr.,* **49**(11–12), 1541–1547.

Prieto, G.A., Parker, R.L., Thomson, D.J., Vernon, F.L. & Graham, R.L., 2007. Reducing the bias of multitaper spectrum estimates, *Geophys. J. Int.,* **171**(3), 1269–1281.

Richmond, A.D., 1995. Modeling equatorial ionospheric electric field, *J. Atmos. Terr. Phys.,* **57,** 1103–1115.

Sanford, T.B., 1971. Motionally induced electric and magnetic fields in the sea, *J. geophys. Res.,* **76**(15), 3476–3492.

Shaw, A. & Tsimplis, M., 2010. The 18.6yr nodal modulation in the tides of Southern European coasts, *Cont. Shelf Res.,* **30**(2), 138–151.

Shimizu, H., Koyama, T., Baba, K. & Utada, H., 2010. Revised 1-D mantle electrical conductivity structure beneath the north Pacific, *Geophys. J. Int.,* **180**(3), 1030–1048.

Thomson, D.J., 1982. Spectrum estimation and harmonic analysis, *Proc. IEEE,* **70**(9), 1055–1096.

Toh, H., 1993. Electrical conductivity structure of the Izu-Bonin arc revealed by seafloor electromagnetic observation, *PhD thesis,* University of Tokyo, Tokyo, Japan.

Toh, H., Hamano, Y. & Ichiki, M., 2006. Long-term seafloor geomagnetic station in the northwest Pacific: a possible candidate for a seafloor geomagnetic observatory, *Earth Planets Space,* **58,** 697–705.

Tyler, R.H., Maus, S. & Lühr, H., 2003. Satellite observations of magnetic fields due to ocean tidal flow, *Science,* **299**(5604), 239–241.

Vivier, F., Maier-Reimer, E. & Tyler, R.H., 2004. Simulations of magnetic fields generated by the Antarctic Circumpolar Current at satellite altitude: can geomagnetic measurements be used to monitor the flow? *Geophys. Res. Lett.,* **31**(10), L10306, doi:10.1029/2004GL019804.

Whittaker, J., Goncharov, A., Williams, S., Dietmar Müller, R. & Leitchenkov, G., 2013. Global sediment thickness dataset updated for the Australian-Antarctic Southern Ocean, *Geochem. Geophys. Geosyst.,* **14**(8), 3297–3305.

APPENDIX A: VARIANCE–COVARIANCE MATRIX OF THE FINAL MODEL COEFFICIENTS

Matrices of the variance–covariance were determined for each station fitting the model defined in eq. (1) for the periods of K2, M2, N2, K1, O1, half a year (HY) and the nodal modulation period (NM). The diagonal values of the matrices show the variance of a coefficient, while the off-diagonals are the covariance between the two estimates. These matrices are shown in Table A1. The components not included in the matrix also had small covariance between them.

As seen from the table, the off diagonal elements (the covariance) are very insignificant compared to the diagonal elements (model variance), implying no significant correlation between the tidal modes.

Table A1. The variance–covariance matrix elements at each station, where *A*, *B*, and *C* are referring to the components from eq. (1) (diagonal values in bold).

NWP	*C*	*A*[K2]	*B*[K2]	*A*[M2]	*B*[M2]	*A*[N2]	*B*[N2]	*A*[K1]	*B*[K1]	*A*[O1]	*B*[O1]	*A*[HY]	*B*[HY]	*A*[NM]	*B*[NM]
C	**9.03E+03**	7.48E-05	1.38E-05	−1.26E-03	6.98E-04	1.41E-04	−8.95E-05	−5.32E-04	−4.85E-05	−1.76E-02	6.91E-03	−4.22E-01	−7.98E-01	4.03E+02	4.82E+02
A[K2]	7.48E-05	**4.10E-04**	−4.97E-09	−2.72E-06	2.27E-06	−2.20E-07	2.04E-07	−1.04E-07	4.68E-08	−1.10E-06	1.12E-06	−1.66E-07	−1.03E-08	5.02E-05	5.60E-05
B[K2]	1.38E-05	−4.97E-09	**4.10E-04**	−2.34E-06	−2.91E-06	−2.02E-07	−2.16E-07	9.54E-09	−3.05E-07	−1.51E-06	−3.12E-06	6.73E-07	−3.74E-07	−2.13E-06	1.98E-05
A[M2]	−1.26E-03	−2.72E-06	−2.34E-06	**4.10E-04**	1.03E-07	−6.52E-06	4.72E-07	7.27E-06	2.24E-06	1.11E-05	1.93E-06	3.54E-07	1.45E-06	−8.09E-04	−9.79E-04
B[M2]	6.98E-04	2.27E-06	−2.91E-06	1.03E-07	**4.10E-04**	−3.33E-07	−6.44E-06	−4.36E-06	2.45E-06	−1.07E-06	1.18E-05	−9.54E-07	−3.98E-07	4.59E-04	5.31E-04
A[N2]	1.41E-04	-2.20E-07	−2.02E-07	−6.52E-06	−3.33E-07	**4.10E-04**	6.82E-09	5.80E-07	1.81E-07	−6.52E-06	−8.65E-07	−3.77E-07	2.66E-08	9.56E-05	1.04E-04
B[N2]	−8.95E-05	2.04E-07	−2.16E-07	4.72E-07	−6.44E-06	6.82E-09	**4.10E-04**	−3.95E-07	1.65E-07	1.57E-06	−6.00E-06	−4.34E-07	3.39E-07	−4.98E-05	−7.56E-05
A[K1]	-5.32E-04	−1.04E-07	9.54E-09	7.27E-06	−4.36E-06	5.80E-07	−3.95E-07	**1.29E-03**	−1.45E-07	3.50E-06	−1.78E-06	1.14E-07	7.15E-08	−3.46E-04	−4.09E-04
B[K1]	−4.85E-05	4.68E-08	−3.05E-07	2.24E-06	2.45E-06	1.81E-07	1.65E-07	−1.45E-07	1.29E-03	1.85E-06	3.72E-06	−6.48E-07	3.55E-07	−3.65E-06	−6.06E-05
A[O1]	−1.76E-02	−1.10E-06	−1.51E-06	1.11E-05	−1.07E-06	−6.52E-06	1.57E-06	3.50E-06	1.85E-06	**4.11E-04**	−2.58E-07	6.82E-06	1.88E-05	−1.13E-02	−1.36E-02
B[O1]	6.91E-03	1.12E-06	−3.12E-06	1.93E-06	1.18E-05	−8.65E-07	−6.00E-06	−1.78E-06	3.72E-06	−2.58E-07	**4.11E-04**	−9.83E-06	−3.60E-06	4.55E-03	5.25E-03
A[HY]	−4.22E-01	−1.66E-07	6.73E-07	3.54E-07	−9.54E-07	−3.77E-07	−4.34E-07	1.14E-07	−6.48E-07	6.82E-06	−9.83E-06	**8.99E-04**	4.30E-04	−2.75E-01	−3.23E-01
B[HY]	−7.98E-01	−1.03E-08	−3.74E-07	1.45E-06	−3.98E-07	2.66E-08	3.39E-07	7.15E-08	3.55E-07	1.88E-05	−3.60E-06	4.30E-04	1.48E-03	−5.12E-01	−6.17E-01
A[NM]	4.03E+02	5.02E-05	−2.13E-06	−8.09E-04	4.59E-04	9.56E-05	−4.98E-05	−3.46E-04	−3.65E-06	−1.13E-02	4.55E-03	−2.75E-01	−5.12E-01	**2.60E+02**	3.11E+02
B[NM]	4.82E+02	5.60E-05	1.98E-05	−9.79E-04	5.31E-04	1.04E-04	−7.56E-05	−4.09E-04	−6.06E-05	−1.36E-02	5.25E-03	−3.23E-01	−6.17E-01	3.11E+02	3.72E+02
C	**1.15E+04**	−9.24E-04	2.25E-03	6.55E-04	−1.32E-03	1.03E-03	−2.54E-03	−2.29E-03	−1.58E-03	−8.63E-03	1.69E-02	3.22E-01	8.40E-01	−3.94E+02	4.29E+02
A[K2]	−9.24E-04	**5.34E-04**	1.80E-08	4.36E-06	−2.89E-06	−1.07E-06	−2.34E-07	6.09E-07	−2.48E-05	−4.82E-07	−2.30E-06	−2.37E-07	−9.25E-07	5.12E-04	−5.55E-04
B[K2]	2.25E-03	1.80E-08	**5.34E-04**	2.85E-06	4.63E-06	3.12E-07	−1.10E-06	1.01E-05	−6.19E-06	3.96E-06	7.63E-07	2.34E-07	3.03E-06	−1.61E-03	1.73E-03
A[M2]	6.55E-04	4.36E-06	2.85E-06	**5.34E-04**	−4.47E-08	8.29E-06	9.57E-06	−2.71E-06	1.08E-05	5.02E-06	−6.19E-06	−1.07E-06	1.16E-06	−4.01E-04	4.01E-04
B[M2]	−1.32E-03	−2.89E-06	4.63E-06	−4.47E-08	**5.34E-04**	−9.47E-06	8.12E-06	−4.01E-06	−3.70E-06	4.67E-06	4.58E-06	−5.66E-08	−1.99E-06	1.03E-03	−1.11E-03
A[N2]	1.03E-03	−1.07E-06	3.12E-07	8.29E-06	−9.47E-06	**5.34E-04**	−6.63E-08	3.26E-07	−3.15E-06	−1.44E-06	−9.23E-06	4.97E-07	9.10E-07	−5.69E-04	6.23E-04
B[N2]	−2.54E-03	−2.34E-07	−1.10E-06	9.57E-06	8.12E-06	−6.63E-08	**5.34E-04**	1.02E-06	−1.67E-06	8.67E-06	−1.97E-06	−2.86E-07	−3.42E-06	1.81E-03	−1.95E-03
A[K1]	−2.29E-03	6.09E-07	1.01E-05	−2.71E-06	−4.01E-06	3.26E-07	1.02E-06	**1.70E-03**	6.86E-06	−4.69E-06	−1.10E-06	−1.58E-07	−3.17E-06	1.59E-03	−1.75E-03
B[K1]	−1.58E-03	−2.48E-05	−6.19E-06	1.08E-05	−3.70E-06	−3.15E-06	−1.67E-06	6.86E-06	**1.65E-03**	6.87E-07	−4.52E-06	−8.62E-08	−8.47E-07	8.11E-04	−8.84E-04
A[O1]	−8.63E-03	−4.82E-07	3.96E-06	5.02E-06	4.67E-06	−1.44E-06	8.67E-06	−4.69E-06	6.87E-07	**5.34E-04**	−4.97E-07	−1.15E-05	−7.59E-06	5.89E-03	−6.63E-03
B[O1]	1.69E-02	−2.30E-06	7.63E-07	−6.19E-06	4.58E-06	−9.23E-06	−1.97E-06	−1.10E-06	−4.52E-06	−4.97E-07	**5.34E-04**	6.11E-06	2.07E-05	−1.15E-02	1.25E-02
A[HY]	3.22E-01	−2.37E-07	2.34E-07	−1.07E-06	−5.66E-08	4.97E-07	−2.86E-07	−1.58E-07	−8.62E-08	−1.15E-05	6.11E-06	**9.46E-04**	3.74E-04	−2.16E-01	2.42E-01
B[HY]	8.40E-01	−9.25E-07	3.03E-06	1.16E-06	−1.99E-06	9.10E-07	−3.42E-06	−3.17E-06	−8.47E-07	−7.59E-06	2.07E-05	3.74E-04	1.77E-03	−5.72E-01	6.20E-01
A[NM]	−3.94E+02	5.12E-04	−1.61E-03	−4.01E-04	1.03E-03	−5.69E-04	1.81E-03	1.59E-03	8.11E-04	5.89E-03	−1.15E-02	−2.16E-01	−5.72E-01	2.68E+02	−2.91E+02
B[NM]	4.29E+02	−5.55E-04	1.73E-03	4.01E-04	−1.11E-03	6.23E-04	−1.95E-03	−1.75E-03	−8.84E-04	−6.63E-03	1.25E-02	2.42E-01	6.20E-01	−2.91E+02	**3.17E+02**

Table A1 *(Continued.)*

T14															
	C	*A*[K2]	*B*[K2]	*A*[M2]	*B*[M2]	*A*[N2]	*B*[N2]	*A*[K1]	*B*[K1]	*A*[O1]	*B*[O1]	*A*[HY]	*B*[HY]	*A*[NM]	*B*[NM]
C	**1.36E+04**	1.02E-03	2.28E-03	−3.04E-03	1.78E-03	−8.99E-04	−3.06E-03	−1.69E-03	1.64E-03	−7.97E-03	−7.74E-03	4.36E-01	7.55E-01	−3.59E+02	3.94E+02
A[K2]	1.02E-03	**6.42E-04**	4.45E-09	9.93E-08	2.73E-06	−3.74E-06	−1.25E-06	8.15E-07	−5.20E-05	6.71E-07	−1.79E-08	1.21E-06	9.25E-07	−7.32E-04	8.19E-04
B[K2]	2.28E-03	4.45E-09	**6.41E-04**	−2.55E-06	9.64E-08	1.08E-06	−3.90E-06	2.08E-05	−6.43E-06	−2.65E-06	1.39E-06	7.72E-07	3.15E-06	−1.61E-03	1.75E-03
A[M2]	−3.04E-03	9.93E-08	−2.55E-06	**6.39E-04**	−1.06E-07	−3.00E-06	9.31E-06	1.41E-06	−7.86E-07	1.73E-06	−5.97E-07	−1.42E-06	−3.68E-06	2.01E-03	−2.19E-03
B[M2]	1.78E-03	2.73E-06	9.64E-08	−1.06E-07	**6.39E-04**	−9.03E-06	−3.30E-06	−5.87E-07	9.86E-06	1.54E-07	−6.06E-08	1.17E-06	2.18E-06	−1.26E-03	1.39E-03
A[N2]	−8.99E-04	−3.74E-06	1.08E-06	−3.00E-06	−9.03E-06	**6.39E-04**	1.30E-08	−5.38E-07	−9.12E-06	−5.68E-06	−2.75E-06	5.27E-07	−1.96E-06	7.45E-04	−7.84E-04
B[N2]	−3.06E-03	−1.25E-06	−3.90E-06	9.31E-06	−3.30E-06	1.30E-08	**6.39E-04**	3.04E-06	−4.33E-06	4.01E-06	−5.95E-06	−1.81E-06	−3.18E-06	1.88E-03	−2.06E-03
A[K1]	−1.69E-03	8.15E-07	2.08E-05	1.41E-06	−5.87E-07	−5.38E-07	3.04E-06	**2.06E-03**	7.43E-06	2.99E-06	−1.96E-06	7.06E-08	−2.83E-06	1.20E-03	−1.33E-03
B[K1]	1.64E-03	−5.20E-05	−6.43E-06	−7.86E-07	9.86E-06	−9.12E-06	−4.33E-06	7.43E-06	**1.96E-03**	2.95E-06	2.62E-06	3.34E-06	1.86E-06	−1.24E-03	1.41E-03
A[O1]	−7.97E-03	6.71E-07	−2.65E-06	1.73E-06	1.54E-07	−5.68E-06	4.01E-06	2.99E-06	2.95E-06	**6.40E-04**	−4.08E-07	−1.35E-05	−3.51E-06	5.22E-03	−5.97E-03
B[O1]	−7.74E-03	−1.79E-08	1.39E-06	−5.97E-07	−6.06E-08	−2.75E-06	−5.95E-06	−1.96E-06	2.62E-06	−4.08E-07	**6.39E-04**	1.58E-06	−1.16E-05	5.22E-03	−5.56E-03
A[HY]	4.36E-01	1.21E-06	7.72E-07	−1.42E-06	1.17E-06	5.27E-07	−1.81E-06	7.06E-08	3.34E-06	−1.35E-05	1.58E-06	**1.19E-03**	4.97E-04	−2.92E-01	3.27E-01
B[HY]	7.55E-01	9.25E-07	3.15E-06	−3.68E-06	2.18E-06	−1.96E-06	−3.18E-06	−2.83E-06	1.86E-06	−3.51E-06	−1.16E-05	4.97E-04	**1.76E-03**	−5.11E-01	5.58E-01
A[NM]	−3.59E+02	−7.32E-04	−1.61E-03	2.01E-03	−1.26E-03	7.45E-04	1.88E-03	1.20E-03	−1.24E-03	5.22E-03	5.22E-03	−2.92E-01	−5.11E-01	**2.42E+02**	−2.66E+02
B[NM]	3.94E+02	8.19E-04	1.75E-03	−2.19E-03	1.39E-03	−7.84E-04	−2.06E-03	−1.33E-03	1.41E-03	−5.97E-03	−5.56E-03	3.27E-01	5.58E-01	−2.66E+02	**2.92E+02**
C	**8.54E+03**	−6.02E-04	1.30E-03	1.60E-03	5.75E-04	1.46E-03	6.33E-04	−1.32E-03	−1.19E-03	2.13E-03	−3.16E-04	1.42E-01	4.93E-01	−2.09E+02	2.27E+02
A[K2]	−6.02E-04	**4.04E-04**	9.93E-08	1.71E-08	4.21E-07	2.89E-08	−9.25E-07	1.09E-06	−3.51E-05	4.87E-07	3.94E-07	−1.83E-07	−5.76E-07	2.95E-04	−3.20E-04
B[K2]	1.30E-03	9.93E-08	**4.04E-04**	−3.94E-07	7.07E-08	9.74E-07	1.71E-07	1.59E-05	−1.12E-05	6.36E-07	3.27E-07	−3.55E-08	1.92E-06	−9.41E-04	1.01E-03
A[M2]	1.60E-03	1.71E-08	−3.94E-07	**4.02E-04**	7.87E-09	3.96E-06	1.21E-06	7.22E-07	4.04E-07	4.81E-08	9.33E-07	1.55E-08	2.33E-06	−1.14E-03	1.23E-03
B[M2]	5.75E-04	4.21E-07	7.07E-08	7.87E-09	**4.02E-04**	−1.11E-06	3.92E-06	7.40E-07	−1.69E-06	−9.42E-07	−4.71E-07	1.35E-07	4.89E-07	−2.58E-04	2.80E-04
A[N2]	1.46E-03	2.89E-08	9.74E-07	3.96E-06	−1.11E-06	**4.02E-04**	8.48E-08	−9.04E-07	1.52E-06	1.62E-06	−2.89E-06	−1.43E-07	2.15E-06	−1.03E-03	1.10E-03
B[N2]	6.33E-04	−9.25E-07	1.71E-07	1.21E-06	3.92E-06	8.48E-08	**4.02E-04**	4.98E-07	−3.25E-06	2.95E-06	7.87E-07	4.75E-07	4.48E-07	−2.86E-04	3.18E-04
A[K1]	−1.32E-03	1.09E-06	1.59E-05	7.22E-07	7.40E-07	−9.04E-07	4.98E-07	**1.30E-03**	1.31E-05	−3.19E-07	−2.41E-08	9.46E-08	−2.04E-06	9.21E-04	−1.02E-03
B[K1]	−1.19E-03	−3.51E-05	−1.12E-05	4.04E-07	−1.69E-06	1.52E-06	−3.25E-06	1.31E-05	**1.23E-03**	−4.02E-08	−5.14E-07	3.46E-08	−5.92E-07	5.44E-04	−5.91E-04
A[O1]	2.13E-03	4.87E-07	6.36E-07	4.81E-08	−9.42E-07	1.62E-06	2.95E-06	−3.19E-07	−4.02E-08	**4.02E-04**	−2.36E-07	7.35E-06	1.44E-07	−1.28E-03	1.55E-03
B[O1]	−3.16E-04	3.94E-07	3.27E-07	9.33E-07	−4.71E-07	−2.89E-06	7.87E-07	−2.41E-08	−5.14E-07	−2.36E-07	**4.02E-04**	−6.47E-06	6.50E-07	2.42E-04	−4.14E-04
A[HY]	1.42E-01	−1.83E-07	−3.55E-08	1.55E-08	1.35E-07	−1.43E-07	4.75E-07	9.46E-08	3.46E-08	7.35E-06	−6.47E-06	**6.11E-04**	1.83E-04	−9.48E-02	1.07E-01
B[HY]	4.93E-01	−5.76E-07	1.92E-06	2.33E-06	4.89E-07	2.15E-06	4.48E-07	−2.04E-06	−5.92E-07	1.44E-07	6.50E-07	1.83E-04	**1.19E-03**	−3.36E-01	3.63E-01
A[NM]	−2.09E+02	2.95E-04	−9.41E-04	−1.14E-03	−2.58E-04	−1.03E-03	−2.86E-04	9.21E-04	5.44E-04	−1.28E-03	2.42E-04	−9.48E-02	−3.36E-01	**1.42E+02**	−1.54E+02
B[NM]	2.27E+02	−3.20E-04	1.01E-03	1.23E-03	2.80E-04	1.10E-03	3.18E-04	−1.02E-03	−5.91E-04	1.55E-03	−4.14E-04	1.07E-01	3.63E-01	−1.54E+02	**1.67E+02**

Table A1 *(Continued.)*

T14															
	C	*A*[K2]	*B*[K2]	*A*[M2]	*B*[M2]	*A*[N2]	*B*[N2]	*A*[K1]	*B*[K1]	*A*[O1]	*B*[O1]	*A*[HY]	*B*[HY]	A[NM]	B[NM]
C	**4.25E+03**	−1.40E-03	5.27E-04	−1.32E-03	−8.14E-04	1.21E-03	8.93E-04	−9.57E-04	−1.45E-03	−2.05E-03	−2.06E-03	−1.25E-01	5.60E-01	−4.34E+02	5.97E+01
A[K2]	−1.40E-03	**1.86E-04**	6.40E-08	1.43E-07	1.96E-07	−2.75E-07	−8.83E-07	−6.23E-08	9.27E-06	7.29E-07	4.74E-07	7.11E-07	−1.32E-06	1.37E-03	−1.79E-04
B[K2]	5.27E-04	6.40E-08	**1.86E-04**	−1.94E-07	2.02E-07	8.89E-07	−3.11E-07	−7.43E-06	7.79E-06	−5.18E-07	5.41E-07	−1.64E-07	6.80E-07	−6.52E-04	8.94E-05
A[M2]	−1.32E-03	1.43E-07	−1.94E-07	**1.86E-04**	−1.45E-08	−2.10E-06	−8.16E-07	2.88E-07	2.42E-07	8.00E-06	−3.38E-06	3.56E-07	−1.43E-06	1.39E-03	−1.90E-04
B[M2]	−8.14E-04	1.96E-07	2.02E-07	−1.45E-08	**1.86E-04**	8.15E-07	−2.10E-06	1.17E-08	−1.60E-07	3.52E-06	7.89E-06	3.39E-07	−6.70E-07	7.08E-04	−9.35E-05
A[N2]	1.21E-03	−2.75E-07	8.89E-07	−2.10E-06	8.15E-07	**1.86E-04**	1.54E-08	−1.08E-06	4.64E-07	−4.90E-07	−1.25E-09	−7.03E-07	1.22E-06	−1.27E-03	1.66E-04
B[N2]	8.93E-04	−8.83E-07	−3.11E-07	−8.16E-07	−2.10E-06	1.54E-08	**1.86E-04**	2.98E-07	−1.49E-06	−2.51E-07	−2.45E-07	−2.35E-07	7.94E-07	−7.83E-04	1.06E-04
A[K1]	−9.57E-04	−6.23E-08	−7.43E-06	2.88E-07	1.17E-08	−1.08E-06	2.98E-07	**5.78E-04**	−9.61E-06	9.26E-07	−5.42E-07	4.36E-07	−1.18E-06	1.08E-03	−1.54E-04
B[K1]	−1.45E-03	9.27E-06	7.79E-06	2.42E-07	−1.60E-07	4.64E-07	−1.49E-06	−9.61E-06	**5.93E-04**	4.75E-07	1.01E-06	6.62E-07	−1.01E-06	1.26E-03	−1.69E-04
A[O1]	−2.05E-03	7.29E-07	−5.18E-07	8.00E-06	3.52E-06	−4.90E-07	−2.51E-07	9.26E-07	4.75E-07	**1.87E-04**	1.06E-07	−5.31E-06	−3.26E-06	1.99E-03	−3.94E-04
B[O1]	−2.06E-03	4.74E-07	5.41E-07	−3.38E-06	7.89E-06	−1.25E-09	−2.45E-07	−5.42E-07	1.01E-06	1.06E-07	**1.86E-04**	1.36E-06	−1.32E-06	1.93E-03	−2.44E-04
A[HY]	−1.25E-01	7.11E-07	−1.64E-07	3.56E-07	3.39E-07	−7.03E-07	−2.35E-07	4.36E-07	6.62E-07	−5.31E-06	1.36E-06	**3.72E-04**	−1.28E-04	1.24E-01	−1.41E-02
B[HY]	5.60E-01	−1.32E-06	6.80E-07	−1.43E-06	−6.70E-07	1.22E-06	7.94E-07	−1.18E-06	−1.01E-06	−3.26E-06	−1.32E-06	−1.28E-04	**9.19E-04**	−5.57E-01	7.73E-02
A[NM]	−4.34E+02	1.37E-03	−6.52E-04	1.39E-03	7.08E-04	−1.27E-03	−7.83E-04	1.08E-03	1.26E-03	1.99E-03	1.93E-03	1.24E-01	−5.57E-01	**4.32E+02**	−5.93E+01
B[NM]	5.97E+01	−1.79E-04	8.94E-05	−1.90E-04	−9.35E-05	1.66E-04	1.06E-04	−1.54E-04	−1.69E-04	−3.94E-04	−2.44E-04	−1.41E-02	7.73E-02	−5.93E+01	**8.22E+00**
C	**7.80E+03**	−1.20E-03	−1.09E-03	−5.04E-04	−1.79E-03	−1.11E-03	−7.33E-04	1.25E-03	−3.10E-03	1.44E-02	7.75E-03	−1.09E-01	8.24E-01	−5.24E+02	2.71E+02
A[K2]	−1.20E-03	**3.52E-04**	1.16E-07	−3.52E-06	−2.32E-06	−2.14E-06	2.19E-07	−9.58E-08	4.07E-06	−2.60E-06	1.90E-06	1.17E-06	−1.30E-06	1.15E-03	−5.74E-04
B[K2]	−1.09E-03	1.16E-07	**3.52E-04**	2.24E-06	−3.57E-06	−4.69E-07	−2.02E-06	−2.71E-06	2.82E-06	1.77E-07	−3.28E-06	−1.17E-06	−1.11E-06	7.38E-04	−4.09E-04
A[M2]	−5.04E-04	−3.52E-06	2.24E-06	**3.53E-04**	−1.02E-07	−2.77E-06	2.43E-06	−2.19E-06	−3.11E-06	7.51E-06	−9.17E-06	−1.08E-06	−9.54E-07	6.20E-04	−3.46E-04
B[M2]	−1.79E-03	−2.32E-06	−3.57E-06	−1.02E-07	**3.53E-04**	−2.51E-06	−2.70E-06	4.39E-06	−8.68E-06	8.23E-06	7.42E-06	7.79E-07	−1.86E-06	1.52E-03	−7.76E-04
A[N2]	−1.11E-03	−2.14E-06	−4.69E-07	−2.77E-06	−2.51E-06	**3.52E-04**	6.29E-08	7.31E-07	−4.04E-06	−4.33E-06	1.13E-07	−5.99E-07	−1.41E-06	1.02E-03	−5.45E-04
B[N2]	−7.33E-04	2.19E-07	−2.02E-06	2.43E-06	−2.70E-06	6.29E-08	**3.52E-04**	2.21E-06	−2.14E-06	−9.99E-07	−3.71E-06	1.73E-06	−5.87E-07	6.48E-04	−3.00E-04
A[K1]	1.25E-03	−9.58E-08	−2.71E-06	−2.19E-06	4.39E-06	7.31E-07	2.21E-06	**1.10E-03**	−2.96E-06	−3.54E-07	4.76E-06	1.71E-06	1.27E-06	−9.40E-04	5.06E-04
B[K1]	−3.10E-03	4.07E-06	2.82E-06	−3.11E-06	−8.68E-06	−4.04E-06	−2.14E-06	−2.96E-06	**1.11E-03**	−4.80E-06	−7.46E-07	6.09E-07	−2.92E-06	2.66E-03	-1.38E-03
A[O1]	1.44E-02	−2.60E-06	1.77E-07	7.51E-06	8.23E-06	−4.33E-06	−9.99E-07	−3.54E-07	−4.80E-06	**3.53E-04**	1.99E-08	−1.72E-06	1.59E-05	−1.27E-02	6.56E-03
B[O1]	7.75E-03	1.90E-06	−3.28E-06	−9.17E-06	7.42E-06	1.13E-07	−3.71E-06	4.76E-06	−7.46E-07	1.99E-08	**3.53E-04**	−1.62E-06	8.97E-06	−7.21E-03	3.72E-03
A[HY]	−1.09E-01	1.17E-06	−1.17E-06	−1.08E-06	7.79E-07	−5.99E-07	1.73E-06	1.71E-06	6.09E-07	−1.72E-06	−1.62E-06	**6.06E-04**	−1.22E-04	9.87E-02	−4.60E-02
B[HY]	8.24E-01	−1.30E-06	−1.11E-06	−9.54E-07	−1.86E-06	−1.41E-06	−5.87E-07	1.27E-06	−2.92E-06	1.59E-05	8.97E-06	−1.22E-04	**1.51E-03**	−7.35E-01	3.80E-01
A[NM]	−5.24E+02	1.15E-03	7.38E-04	6.20E-04	1.52E-03	1.02E-03	6.48E-04	−9.40E-04	2.66E-03	−1.27E-02	−7.21E-03	9.87E-02	−7.35E-01	**4.68E+02**	−2.42E+02
B[NM]	2.71E+02	−5.74E-04	−4.09E-04	−3.46E-04	−7.76E-04	−5.45E-04	−3.00E-04	5.06E-04	−1.38E-03	6.56E-03	3.72E-03	−4.60E-02	3.80E-01	−2.42E+02	**1.25E+02**